

We are IntechOpen, the world's leading publisher of Open Access books Built by scientists, for scientists

6,900

Open access books available

185,000

International authors and editors

200M

Downloads

Our authors are among the

154

Countries delivered to

TOP 1%

most cited scientists

12.2%

Contributors from top 500 universities



WEB OF SCIENCE™

Selection of our books indexed in the Book Citation Index
in Web of Science™ Core Collection (BKCI)

Interested in publishing with us?
Contact book.department@intechopen.com

Numbers displayed above are based on latest data collected.
For more information visit www.intechopen.com



Conjugate Heat Transfer in Ribbed Cylindrical Channels

Armando Gallegos-Muñoz, Nicolás C. Uzárraga-Rodríguez
and Francisco Elizalde-Blancas

Additional information is available at the end of the chapter

<http://dx.doi.org/10.5772/49942>

1. Introduction

In the last years, many technological advances have emerged in the turbo machinery industry, mainly in the area of power generation using gas turbines [1]. The main target in this science field consists on designing and building more efficient machines with a higher life-time by means of applied research. However, in order to achieve this, it is necessary that the gas turbine operates at high compression pressure ratios as well as high turbine inlet temperatures (TIT), but these operating conditions generate thermal consequences or degradations in the gas turbine components that are exposed to the high temperatures, like blades and vanes of the first stage. For this reason, it is necessary to have an internal cooling system in gas turbines to avoid the reduction of the useful life of their hot components, since the useful life of turbine blades is reduced to half with every 10 – 15 °C rise in metal temperature [2]. Nowadays basic methods exist, which improve the gas turbines operating conditions, having as a result improvements of the external cooling [3], where the use of micro-jets with smaller diameters enhanced the overall heat transfer coefficient, or internal cooling where square ribbed channels are employed to study the thermal behaviour of the flow inside the channel [4], turbulence promoters with different geometries to study the temperature distribution in the gas turbine blades [5]. Also, it is possible using serpentine passages inside the turbine blade to improve internal convective cooling [6], ribs in the internal surface of the cooling passages where the rib-to-rib pitch and angle of attack that yield a maximum heat transfer and maximum thermal performance are determined [7] or ribs as turbulence promoters to increase the rate of heat transfer [8]. To increase the heat transfer with minimal friction in compact heat exchangers, the internal surfaces are ribbed with protuberances that have convex and concave forms [9]. To study the heat transfer characteristics of laminar flow in parallel-plate dimpled channels are used [10] or square-channel fitted with baffles [11].

However, a common way to increase the internal cooling efficiency in gas turbines is to add ribs, this method offers a better mixed fluid near to the hot internal surface of the channel thus increasing the thermal heat transfer. The present study shows a numerical analysis of the first stage blades in a gas turbine with internal cooling system (model MS7001E) applying the conjugated heat transfer. This method considers the direct coupling of fluid flow and solid body using the same mesh distribution and numerical principles for both domains. This coupling is achieved by using boundary conditions called double-side wall.

2. Mathematical formulation

The numerical analysis of a gas turbine at first stage blade with internal cooling system considers the solution of the conjugate heat transfer in steady state between the hot combustion gases flowing around the blade and the coolant flowing inside the cooling channels of gas turbine blades. The following assumptions are made to model the conjugate heat transfer problem:

- a. Newtonian fluid,
- b. Compressible and turbulent flow
- c. Rotational frame with relative velocity formulation
- d. Fluid is considered as an ideal gas.

2.1. Governing equations

The applied governing equations are the 3D Reynolds-averaged Navier-Stokes equations [12], which were solved by commercial Computational Fluid Dynamics software [13]. The governing equations solved by the model are:

Continuity equation

$$\frac{\partial}{\partial x_i} (\overline{\rho u_i} + \overline{\rho' u_i'}) = 0 \quad (1)$$

Momentum equation

$$\frac{\partial}{\partial x_j} (\overline{\rho u_i u_j}) = \rho \bar{g}_i - \frac{\partial p}{\partial x_i} + \frac{\partial (\tau_{ij})}{\partial x_j} + F_i \quad (2)$$

where F_i is the source term which includes contributions due to the body force. Assuming constant rotational velocity with relative velocity formulation, the source terms due to rotation are:

$$a^{co} = 2\bar{\omega} \times \bar{u}_i \quad \text{and} \quad a^{ce} = \bar{\omega} \times \bar{\omega} \times \bar{r} \quad (3)$$

The term τ_{ij} is the stress tensor, which is expressed as:

$$\tau_{ij} = \mu \left(\frac{\partial \bar{u}_i}{\partial x_j} + \frac{\partial \bar{u}_j}{\partial x_i} - \frac{2}{3} \delta_{ij} \frac{\partial \bar{u}_k}{\partial x_k} \right) - \rho \overline{u'_i u'_j} \quad (4)$$

Energy equations

The energy equation for the fluid domain is given by

$$\frac{\partial}{\partial x_i} (\rho C_P u_i T) = \frac{\partial}{\partial x_i} \left[C_P \frac{\mu}{Pr} \frac{\partial T}{\partial x_i} + \rho C_P \overline{u'_i T'} \right] + \mu \phi \quad (5)$$

where $\mu\phi$ is the viscous heating dissipation and $\rho C_P \overline{u'_i T'}$ represents the turbulent heat flux. The energy conservation equation for the solid is given by the conductive term in the energy equation. In the solid continuum, only the heat flux due to conduction is included inside itself. This is described by the heat diffusion equation:

$$\frac{\partial}{\partial x_i} \left(\lambda_{solid} \frac{\partial T_{solid}}{\partial x_i} \right) = 0 \quad (6)$$

where λ_{solid} is the thermal conductivity. Equations (5) and (6) are solved simultaneously by a conjugate heat transfer analysis. This permits to yield a fully coupled conduction-convection heat transfer prediction.

Turbulence model

Since the behaviour of the flow in the gas turbine is very chaotic, it is necessary to incorporate a turbulence model in the numerical analysis to determine the Reynolds stresses. The Standard k - ϵ model was used, which relates the Reynolds stresses to the mean velocity by the Boussinesq hypothesis [13]:

$$-\overline{u'_i u'_j} = \mu_t \left(\frac{\partial \bar{u}_i}{\partial x_j} + \frac{\partial \bar{u}_j}{\partial x_i} \right) - \frac{2}{3} \left(\rho k + \mu_t \frac{\partial \bar{u}_k}{\partial x_k} \right) \delta_{ij} \quad (7)$$

The eddy turbulent viscosity, μ_t , is calculated by the combination of the turbulent kinetic energy (k) and the dissipation ratio (ϵ), as shown by equation (8).

$$\mu_t = \rho \cdot C_\mu \cdot \frac{k^2}{\epsilon} \quad (8)$$

where C_μ is a constant. This model offers a reasonable accuracy for a wide range of turbulent flows in practical engineering problems, in which the turbulent kinetic energy, k , and its dissipation ratio, ϵ , are obtained from the following transport equations:

$$\frac{\partial}{\partial x_i} (\rho k u_i) = \frac{\partial}{\partial x_j} \left[\left(\mu + \frac{\mu_t}{\sigma_k} \right) \frac{\partial k}{\partial x_j} \right] + G_k + G_b - \rho \epsilon - Y_m \quad (9)$$

$$\frac{\partial}{\partial x_i}(\rho \varepsilon u_i) = \frac{\partial}{\partial x_j} \left[\left(\mu + \frac{\mu_t}{\sigma_\varepsilon} \right) \frac{\partial \varepsilon}{\partial x_j} \right] + C_{1\varepsilon} \frac{\varepsilon}{k} (G_k + C_{3\varepsilon} G_b) - C_{2\varepsilon} \rho \frac{\varepsilon^2}{k} \quad (10)$$

In these equations, G_k represents the generation of turbulent kinetic energy due to the mean velocity gradients, G_b is the generation of turbulent kinetic energy due to buoyancy, and the quantities σ_k and σ_ε are the turbulent Prandtl numbers for k and ε , respectively. The empirical constants appearing in the above equations take the following values: $C_\mu = 0.09$, $C_{1\varepsilon} = 1.44$, $C_{2\varepsilon} = 1.92$, $\sigma_k = 1.0$ and $\sigma_\varepsilon = 1.3$ [13].

Equation of state

The density variation in both fluids, the hot combustion gases and cooling air, is assumed according to the gas ideal law:

$$\rho = \frac{P_{op} + P}{RT} \quad (11)$$

where R is the gas constant. This equation of state provides the linkage between the energy equation on one side, and the mass conservation and moment equations on the other. This linkage emerges from the density variations.

2.2. Computational model and grid

The computational model and mesh were generated in the pre-processor GAMBIT [14]. In order to avoid many simplifications in the computational model, such as the use of boundary conditions at surfaces and outlets of the cooling channels, the computational model was generated using the total blade geometry, which includes the plenum, gap in the tip, gaps between the seal and the plenum and the ribbed cooling channels. Figure 1 shows the rotor blade geometry at the first stage of the gas turbine MS7001E.

In this Figure the internal cooling system can be seen. This system has 13 cylindrical channels inside the blade. The ribs were placed on the inner surface of the cooling channels in order to increase the heat transfer from the solid body to the cooling air. Also, in Figure 1 can be seen that the ribs were only placed in the middle blade zone inside the cooling channels; because in this zone the largest temperature gradient is present [15], causing failure such as cracks in the blade structure [16].

Three different geometries of rib configurations are studied, which are square, triangular and semi-circular forms. The ribs are placed perpendicularly to the air flow. Figure 2 shows a sketch of the different rib parameters used in the square cross-section ribs. These parameters are used for the other two geometries (triangular and semi-circular). Moreover, these configurations are applied for both arrangements (full and half-ribs). Figure 3 shows the form and parameters of the ribs cross-section.

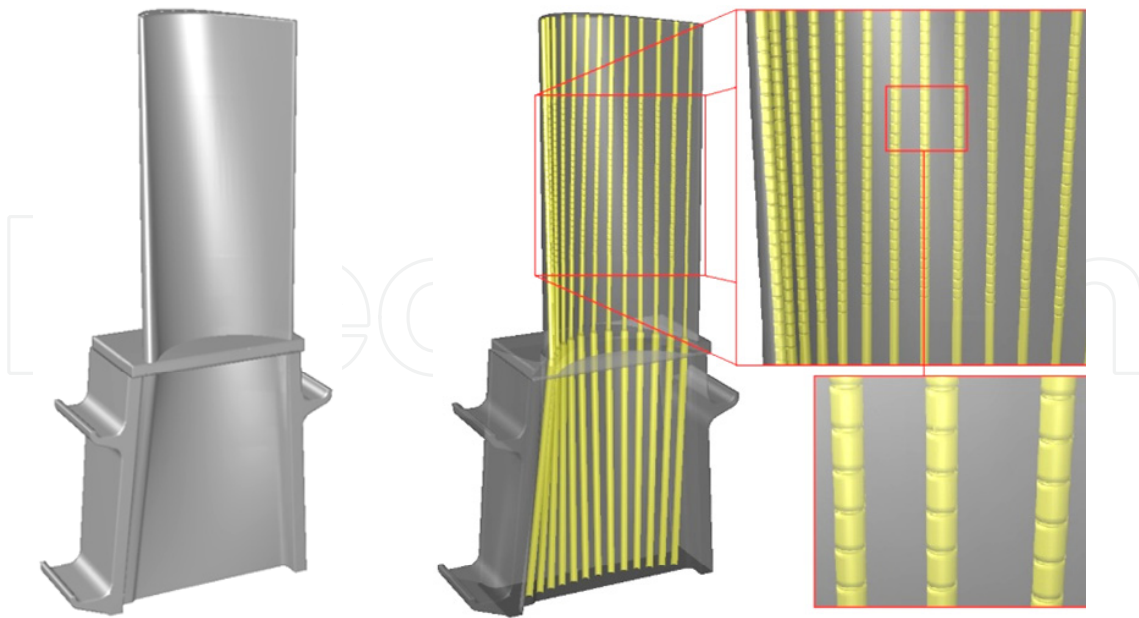


Figure 1. Blade geometry with plenum and its internal features (ribbed cooling channels)

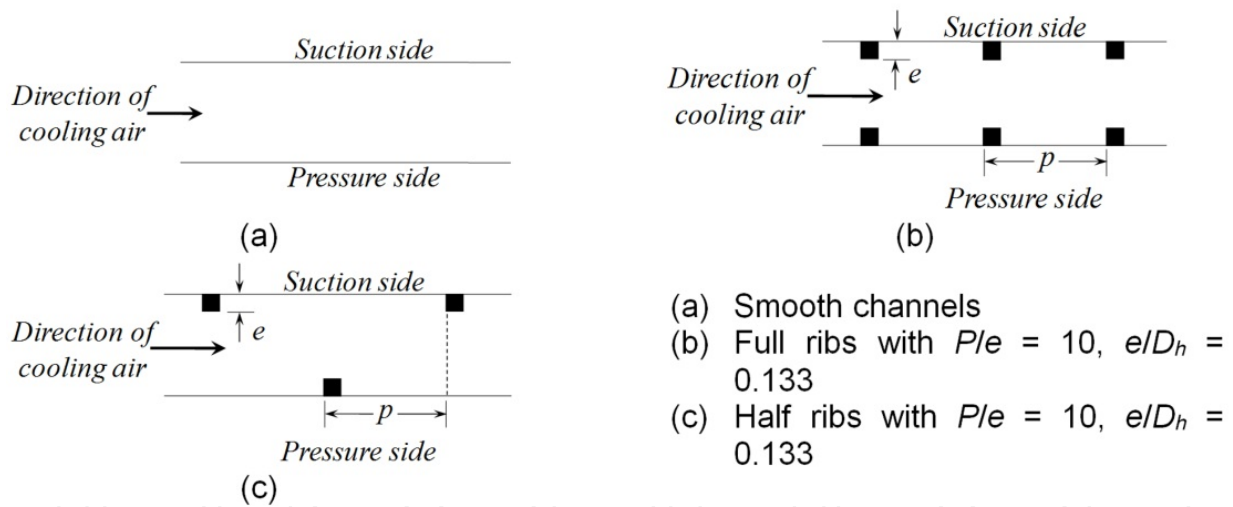


Figure 2. Sketch of different arrays to study the effect of the ribs

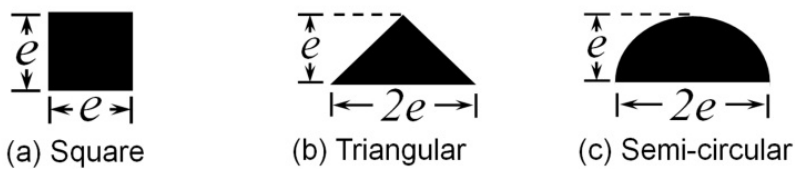


Figure 3. Cross-section of the ribs

Due to complexity of the geometry, different computational grid sizes are required. These grids are not uniform in all directions and were structured by mixing different types of cells (hexahedral and prismatic elements). For the grid used in the blade computational model with smooth cooling channels, the mesh density is high in the near-wall region of the blade

body. The first wall-adjacent cells height in the vicinity of regions corresponding to the leading and trailing edge as well as in the suction and pressure side of the blade is 0.0012 mm, while in the region corresponding to the internal cooling channels, the wall-adjacent cell height is 0.0035 mm. This is developed in order to get a better solution into the boundary layer, obtaining y^+ values closer to unity along the surfaces (ranging from 1 to 5.5). An analysis to evaluate the grid independence of the numerical solution was developed. The computational grid has a total of 3809734 mixed cells, 80% of this total corresponding to fluid (33% air and 47% hot gases) and 20% to solid. Figure 4 shows the grid used in this case. It can be observed, that the hot combustion gases domain presents a high quantity of hexahedral elements.

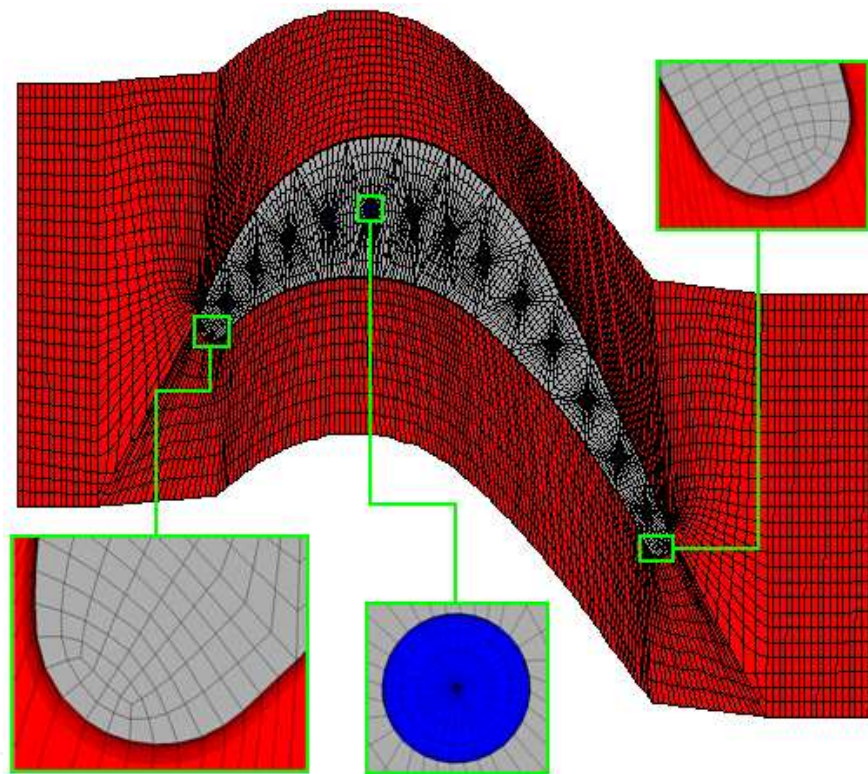


Figure 4. Computational grid for hot combustion gas (red), blade (gray) and cooling air (blue) domains

For the blade models with ribbed cooling channels, the same grid distribution was used at the region of hot combustion gases and the external blade surface. The height of the first wall-adjacent cells in the vicinity of regions corresponding to ribbed cooling channels was of 0.002 mm, obtaining y^+ values less than 5 for all the analyzed rib configurations. The computational grid used ranges from 6.5 to 7.5 million of mixed cells. Figure 5 shows the grids used in the internal cooling channels with full-ribs having an aspect ratio of $P/e = 10$.

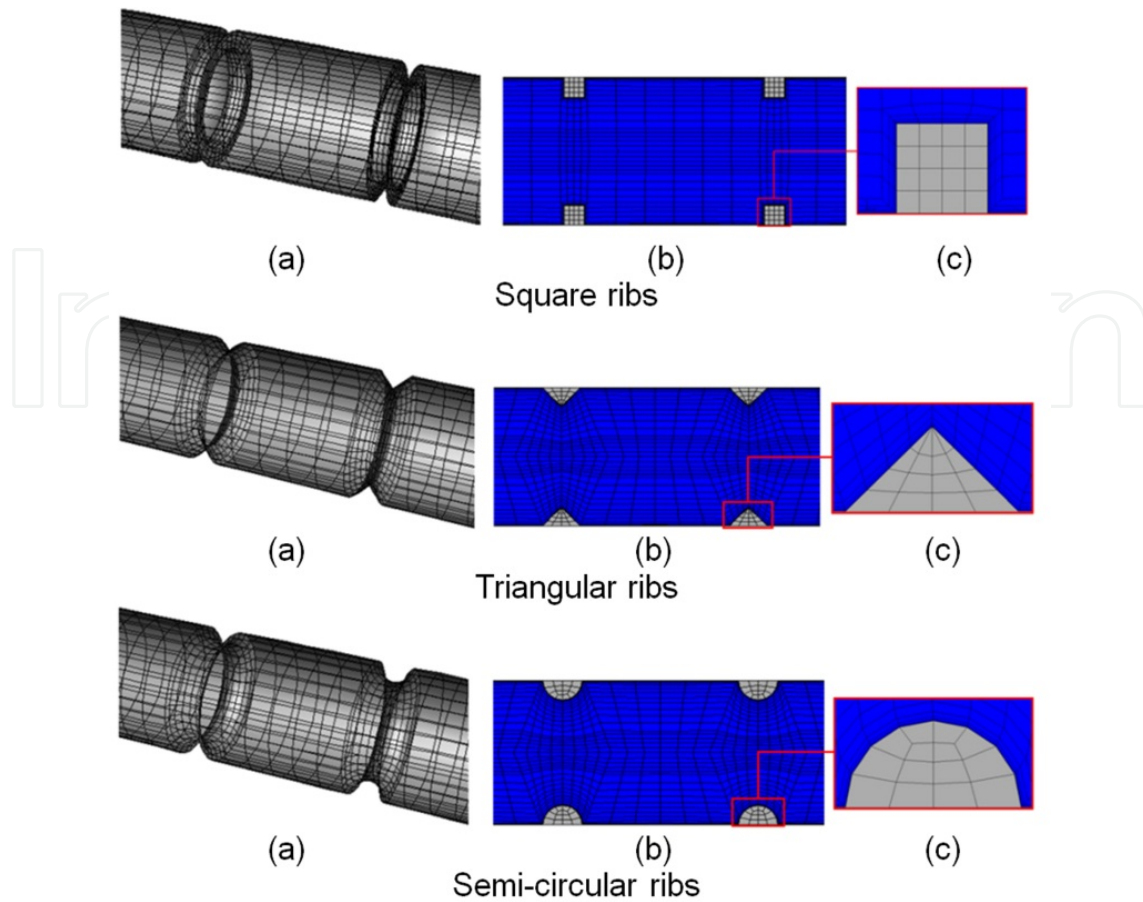


Figure 5. Computational grid for cooling channels domain with full-ribs with $P/e = 10$. (a) channels and surfaces, (b) cooling air and (c) ribs

For the models with half-ribs, it was used the same grid distribution showed in the Figure 5, having a small variation in the ribs domains, defining one half of the domain as fluid and the other half as solid. Figure 6 shows the grid used in the internal cooling channels with half-ribs having an aspect ratio of $P/e = 10$.

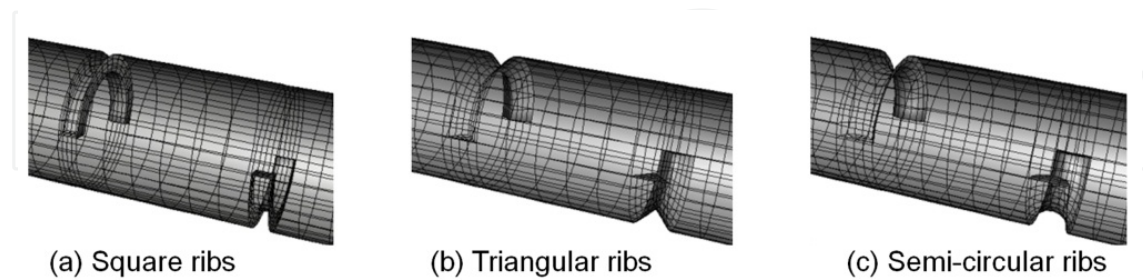


Figure 6. Computational grid for cooling channels domain with half-ribs with $P/e = 10$

2.3. Boundary conditions and thermal properties

The boundary conditions used for the computational model with smooth cooling channels are defined according to approximate values of the gas turbine operating conditions in steady state. Figure 7 shows the boundary conditions used in the computational model.

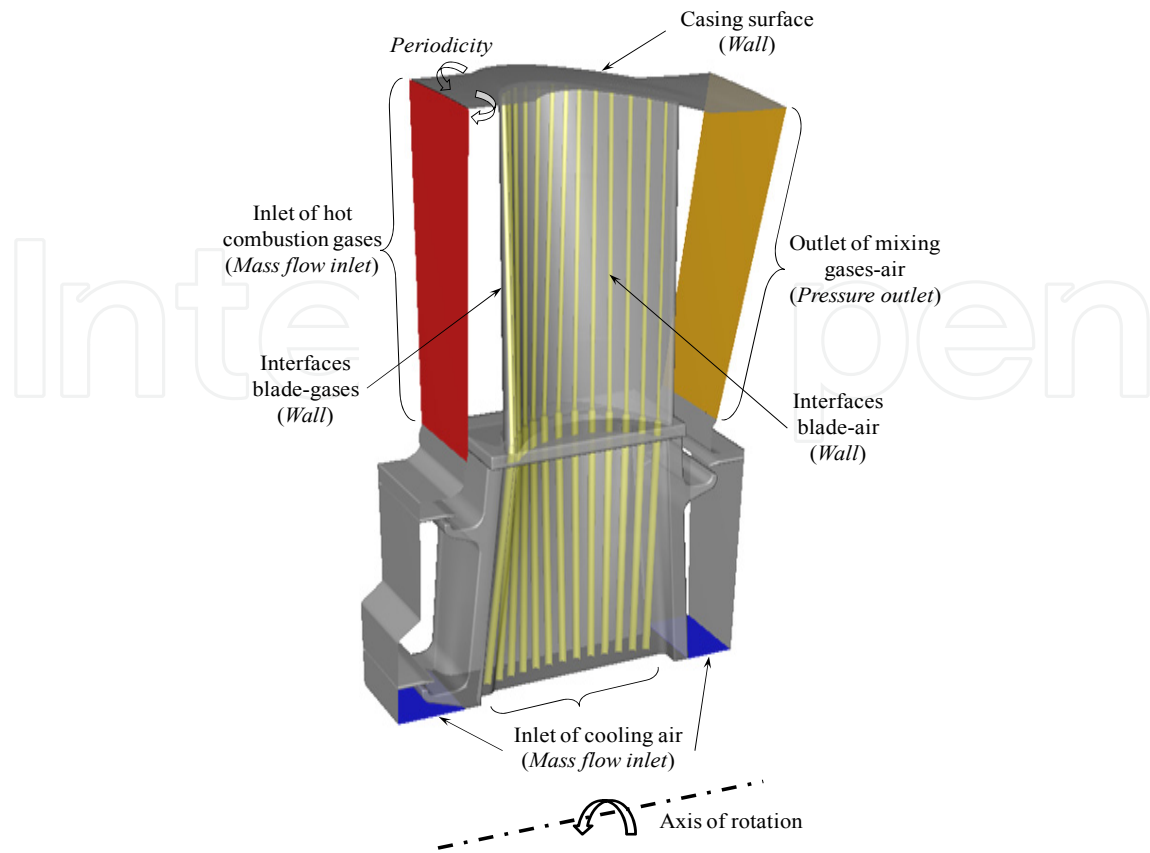


Figure 7. Boundary conditions in the model of a gas turbine blade

In the hot combustion gases inlet, the operational conditions are: mass flow of 2.47 kg/s, static pressure of 508700 Pa and total temperature profile is a function of the radial coordinate. This total temperature profile is described by the next equation [17]:

$$T(r) = -662195 r^4 + 2 \times 10^6 r^3 - 3 \times 10^6 r^2 + 2 \times 10^6 r - 435431 \quad (12)$$

This total temperature profile is imposed in order to match the oxidation mark of hot combustion gases over the airfoil of the blade, which has been operating until the end of its useful life [18], and because this profile is similar to the one obtained in the radial edge direction of the exit of the transition piece. Figure 8 shows the oxidation marks on the blade.

The units for the independent variables of Equation 12 are: (m) for the rotational radius and (K) for the total temperature. The turbulence quantities at the inlet of the model are defined using a turbulence intensity of 5% and 0.006 m for turbulent length scale.

A mass flow of 0.0048 kg/s of air, a static pressure of 897300 Pa, and a total temperature of 853.15 K were specified for each inlet zones of the thirteen cooling channels. Also, turbulence parameters are defined using a turbulence intensity of 5% and a hydraulic diameter of 0.004 m for these boundaries. At the left and right sides of the plenum inlets of cooling air were adjusted with a mass flow of 0.152 kg/s and 0.025 kg/s, respectively. As well, a turbulence intensity of 5% and turbulent length scale of 0.005 m was set. In the remaining inlet section of the cooling plenum, boundary conditions were adjusted to the

same conditions used at the inlets of the cooling channels for the parameters of pressure and temperature. At the exit of the gas-air mixture a static pressure of 473170 Pa, and a backflow total temperature of 1226 K were specified.



Figure 8. Oxidation (corrosion) marks on the blade [18].

For the solid surfaces the conditions were imposed as no-slip condition, while for the thermal condition were imposed as coupled. With these considerations it is possible to solve simultaneously the solid-fluid interfaces. At the interfaces, the temperature and heat flux could be continuous. These conditions are developed by the use of the boundary conditions denominated as two-side wall, which can be expressed as:

$$T_{fluid} = T_{solid} \quad (13)$$

$$\lambda_{fluid} \frac{\partial T}{\partial n} \Big|_{fluid} = \lambda_{solid} \frac{\partial T}{\partial n} \Big|_{solid} \quad (14)$$

Rotational periodic boundary conditions are defined for the suction and pressure side of the computational model and a nominal angular velocity vector were prescribed.

The flow and heat transfer analysis were performed under the assumption that the fluid behaviour is compressible and viscous. For the case of the air properties, these are temperature dependant, while the thermo-physical properties of the solid domain were assumed to behave like Inconel 738LC alloy. The thermo-physical properties of the fluid and solid domains are showed in Table 1 [19] and Table 2 [18], respectively.

T	C _p	$\lambda \cdot 10^3$	$\mu \cdot 10^6$
[K]	[kJ/kg·K]	[W/m·K]	[N·s/m ²]
200	1.007	18.1	13.25
300	1.007	26.3	18.46
400	1.014	33.8	23.01
500	1.030	40.7	27.01
600	1.051	46.9	30.58
700	1.075	52.4	33.88
800	1.099	57.3	36.98
900	1.121	62.0	39.81
1000	1.141	66.7	42.44
1100	1.159	71.5	44.90
1200	1.175	76.3	47.30
1300	1.189	82	49.6
1400	1.207	91	53.0

Table 1. Fluid properties

T	C _p	λ	ρ
[K]	[J/kg·K]	[W/m·K]	[kg/m ³]
294.260	420.100	11.83	8110
366.480	462.110	11.83	8110
477.590	504.120	11.83	8110
588.700	525.120	13.70	8110
699.810	546.130	15.58	8110
810.920	567.130	17.74	8110
922.030	588.140	19.76	8110
1033.150	630.150	21.50	8110
1144.260	672.160	23.37	8110
1255.370	714.170	25.39	8110
1366.480	714.170	27.27	8110

Table 2. Properties of Inconel 738LC alloy

2.4. Numerical method

Fluid flow and turbulent heat transfer analysis of the first stage gas turbine blade (MS7001E) with different ribs configurations placed in the internal cooling channels were realized using commercial Computational Fluid Dynamic software (FLUENT®). This code allows to solve the Reynolds averaged Navier-Stokes and the transport equations of the turbulent quantities for the compressible viscous flow. This CFD code solves the equations using the finite volume technique [20] to discretize the governing equations inside the computational domains. The Standard k - ϵ model [21] was used for all numerical simulations. This model is a semi-empirical linear eddy viscosity model based on the transport equations for the

turbulent kinetic energy (k) and dissipation rate (ϵ). The model transport equation for k is derived from the exact equation, while the model transport equation for ϵ is obtained using physical reasoning and little resemblance to its mathematically exact counterpart. The SIMPLE algorithm was used to link the velocity field and pressure distribution inside the computational model. This algorithm uses a relation between the velocity and pressure in order to satisfy the mass conservation, getting a velocity field. The SIMPLE algorithm along with the implicit time treatment of the flow variables allow to obtain a steady solution or use rather time steps for unsteady flow computations [13].

The governing equations were solved simultaneously by the approach of the pressure-based solver. The pressure-based approach is recommended in the literature [13] to be used for flows with moderate compressibility, since it offers a better convergence. Due to the fact that the governing equations are non-linear and coupled, several iterations were needed to reach a converged solution. The Gauss-Seidel linear algorithm was used to solve the set of algebraic equations obtained by the discretization in FLUENT®. The convergence was reached when the residuals of the velocity components in the Reynolds averaged Navier-Stokes equations, continuity and turbulent quantities were smaller than 10^{-5} , while for the energy conservation equation the residuals were smaller than 10^{-6} .

Six computational equipments were used to solve the model. Each computer has a 3 GHz processor and 2 GB in RAM. These equipments were connected in a scheme of parallel processing. Figure 9 shows a sketch of the parallel processing equipment using a basic LAN topology.

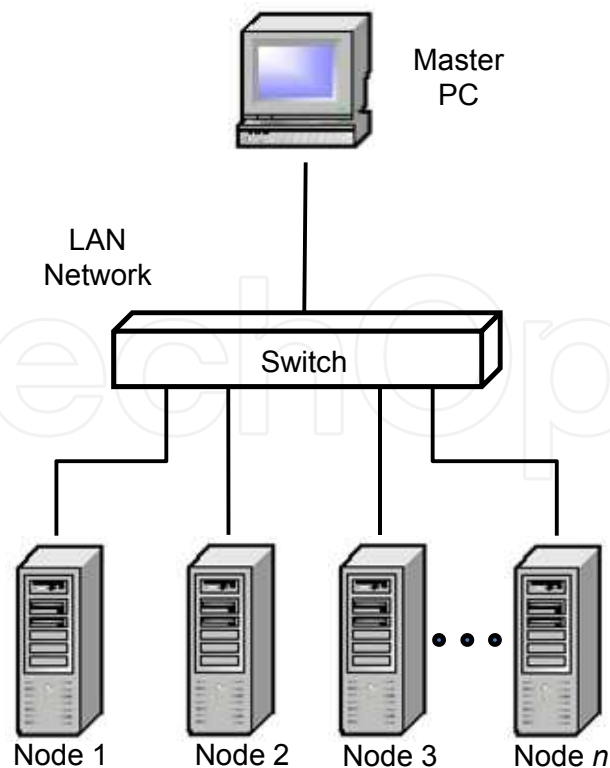


Figure 9. Sketch of parallel processing.

3. Results and discussions

In the first part, a comparison between the results obtained experimentally by Kwak [22] and numerically for the external flow is presented. Also, a comparison between results obtained from semi-empirical correlations derived from the *law of the wall* [23] and the numerical results of the internal flow are presented. In the second part the effects on internal flow through the internal cooling channels are presented. Finally, the temperature distribution inside the blade body and the surface temperature distribution in the blade body with and without ribs are showed.

3.1. Comparison with experimental and semi-empirical correlation data

In order to validate the external flow around the blade a qualitative comparison between the pressure distribution obtained numerically and experimentally [22], has been performed. In [22] the pressure distribution on the gas turbine blade of GE-E3 was measured. Figure 10 shows the comparison between the numerical and experimental pressure distribution at the middle of the blade. Several turbulence models were used. The turbulence models used in the comparison were Standard $k-\varepsilon$, RNG $k-\varepsilon$ and SST $k-\omega$ models, which are known as two-equation eddy viscosity models (EVMs). The total inlet pressure and local static pressure around the blade (p_0/p_s) are plotted as a function of x/C_x , where x is the axial length measured from the leading edge (LE) of the blade, considered as the characteristic length.

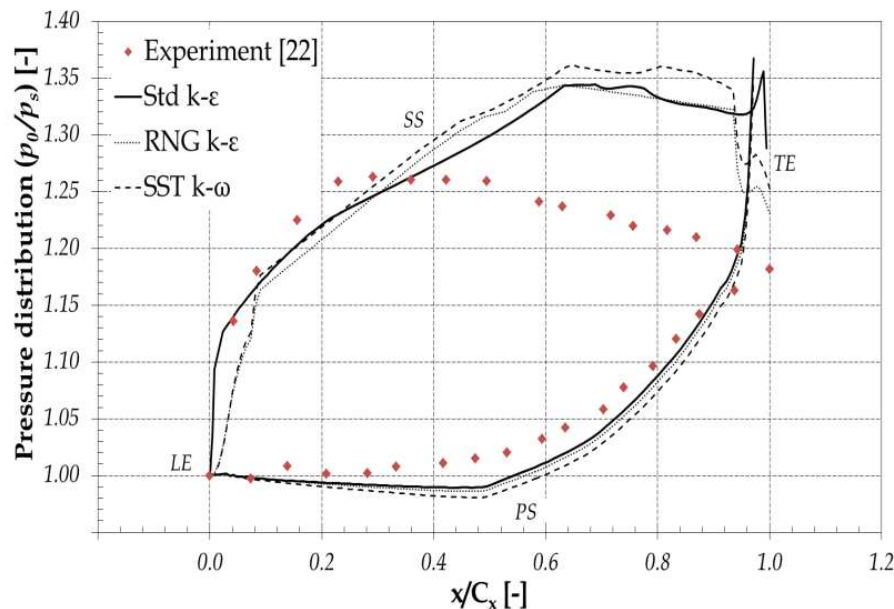


Figure 10. Pressure distribution around the blade

In Figure 10 can be seen that the pressure distribution, p_0/p_s , corresponding to numerical solution on the pressure side (PS) of the blade, agrees with the experimental data. While some differences for the pressure distribution, p_0/p_s , on the suction side (SS) of the blade, are observed.

For comparison purposes of the internal flow in the cooling channels, the pressure drop given by the section with square full-ribs having an aspect ratio of $P/e = 10$ for the central cooling channel was determined. This pressure drop was calculated by the friction factor for ribbed tubes, using semi-empirical correlations derived from the law of wall. Nikuradse [23] developed a friction factor correlation to be used in geometries with sand-grain roughness. His results were excellent for a wide range of roughness sizes. This correlation is expressed by Equation (15).

$$R(e^+) = \sqrt{2/f} + 2.5 \ln(2e/D_h) + 3.75 \quad (15)$$

The term $e^+ = eu^*/v$ is the roughness Reynolds number and D_h is the hydraulic diameter which can be expressed as:

$$D_h = \frac{4A}{P_w} \quad (16)$$

where A is the cross section area and P_w is the wetted perimeter of the cooling channel. Webb [24] used Equation (15) to calculate frictional data for turbulent flows in ribbed tubes with circular cross-section, obtaining excellent results. They found that the roughness function could be correlated as Equation (17).

$$R(e^+) = 0.95(P/e)^{0.53} \quad (17)$$

This equation is valid in the range $e^+ > 35$. By solving Equations (15) and (17) the friction factor can be found from the geometrical parameters of the internal structure of the ribbed channels. Equation (18) shows the result obtained.

$$f = \frac{2}{\left[R - (2.5 \ln(2e/D_h) + 3.75) \right]^2} \quad (18)$$

Equation (18) is valid for channels with ribs placed 90° to the flow direction and an aspect ratio of $P/e = 10$. Table 3 shows the pressure drop calculated by the Equation (18) and the numerical results obtained in this work.

	Correlation Eq. (18)	Numeric
Δp (kPa)	3893.90	3917.20

Table 3. Pressure drop comparison between analytical and numerical results

The pressure drop calculated numerically presents a good approximation, having an absolute difference of 3.25%.

3.2. Effects of the internal flow through internal cooling channels

In order to determine the effects generated by the ribs, a line along the central cooling channel was created. This centerline is dimensionless with a range from 0 to 1, where y is the

dimensionless distance of the axial length of the internal cooling channel, measured from the base of the blade until the outlet of the cooling channel. This centerline was used to obtain data of the flow parameters, such as temperature, velocity, Mach number and pressure loss.

Temperature distribution

Figure 11 shows the temperature distributions of the coolant flow along the centerline of the central cooling channels. Figures 11a and 11c show the results for different types of full-ribs, and Figures 11b, and 11d show the results for the half-ribs studies, having a ratio of $P/e = 10$ and $P/e = 20$, respectively. The higher and smaller temperatures are presented for the configurations of full-ribs in the ribbed section (Figs. 11a and 11c.), reaching temperatures from 937 K to 741 K, respectively. While the half-ribs configurations offer a smaller difference of temperature in this section. This range is between temperature values of 927 K and 791 K. As can be seen in Figure 11, the temperature presents a moderate increase at the smooth inlet section. In the ribbed section, the temperature presents a periodic variation, due to the acceleration and deceleration of the flow inside the cooling channels caused by the presence of the ribs. At the end of the ribbed section, the temperature strongly decreases. This effect is similar to compressible flow with heat transfer (Rayleigh curve) [25], where the temperature decreases to reach a Mach number larger than one. In the smooth outlet section, the temperature increases at the beginning of the section, due to the decrement in the Mach number. The temperature suffers a decrement while the flow gets closer to the outlet channel.

The temperature contours along the central cooling channel at a longitudinal plane are shown in Figure 12. Figures 12a, 12c and 12e show the results for different types of full-ribs, and Figures 12b, 12d and 12f show results for the half-ribs, both models have a ratio of $P/e = 10$. The fluid temperature increases while it goes along the channel for all cases (arrow indicates the direction of flow). The surface temperature of the channels is higher in the cases with half-ribs. Thus, the flow is heated at surface near the ribs. For the cases with full-ribs, the surface temperature is lower, showing a more uniform temperature distribution near to the wall.

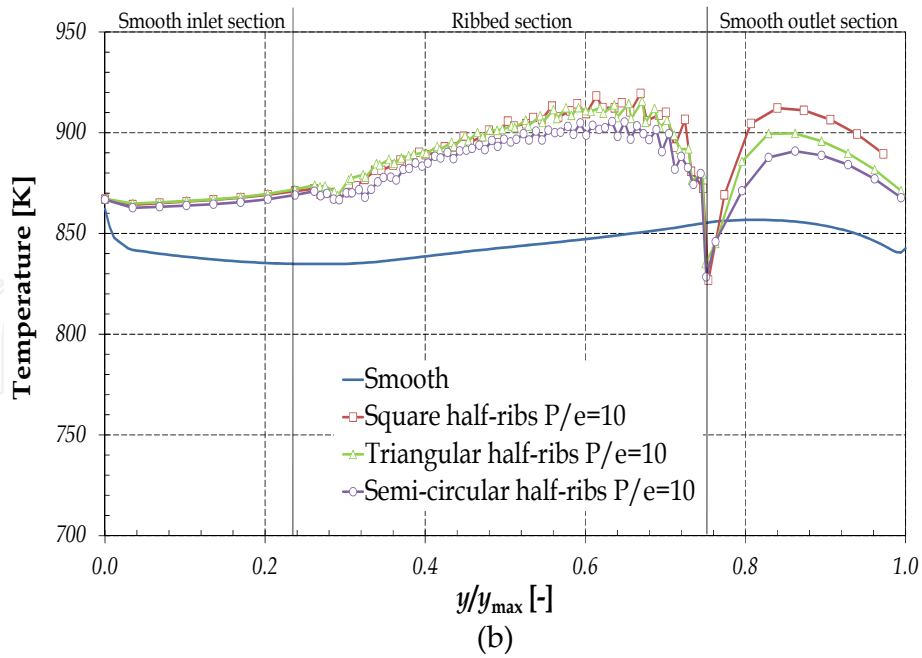
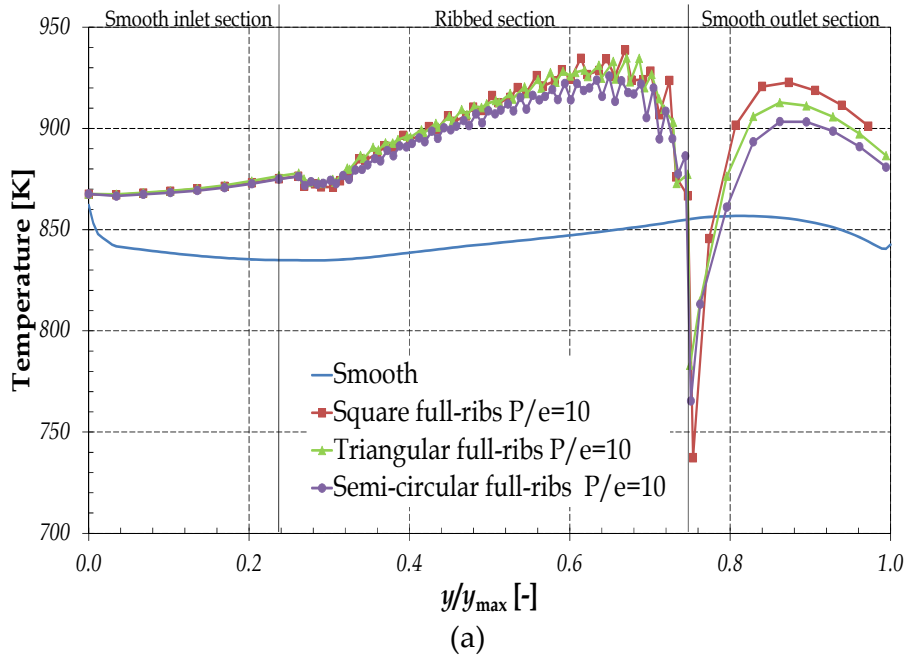
The triangular ribs configuration presents the lowest temperatures, because this configuration offers the best cooling design inside the blade body. These effects are similar to the configurations with ribs whose $P/e = 20$.

Velocity and mach number distribution

Figure 13 shows the comparison between velocity magnitude and Mach number distributions obtained for the cases of blades with smooth and ribbed channels.

In the ribbed channel corresponding to the configuration of square full-ribs with an aspect ratio of $P/e = 10$, the highest Mach number and velocity are obtained, whose values are 1.45 and 823 m/s, respectively. The smooth channel presents a continuous acceleration of the flow through the channels. In the case of the ribbed channel, the flow is moderately accelerated in the smooth inlet section. The flow becomes unstable in the ribbed section; experiencing acceleration and deceleration continuously. At the end of this section, in the last rib, the flow is strongly accelerated as can be seen in Figure 13. High velocities decrease

at the beginning of smooth outlet section, and then accelerate again towards the outlet of the smooth channel. This effect is due to the rotational force.



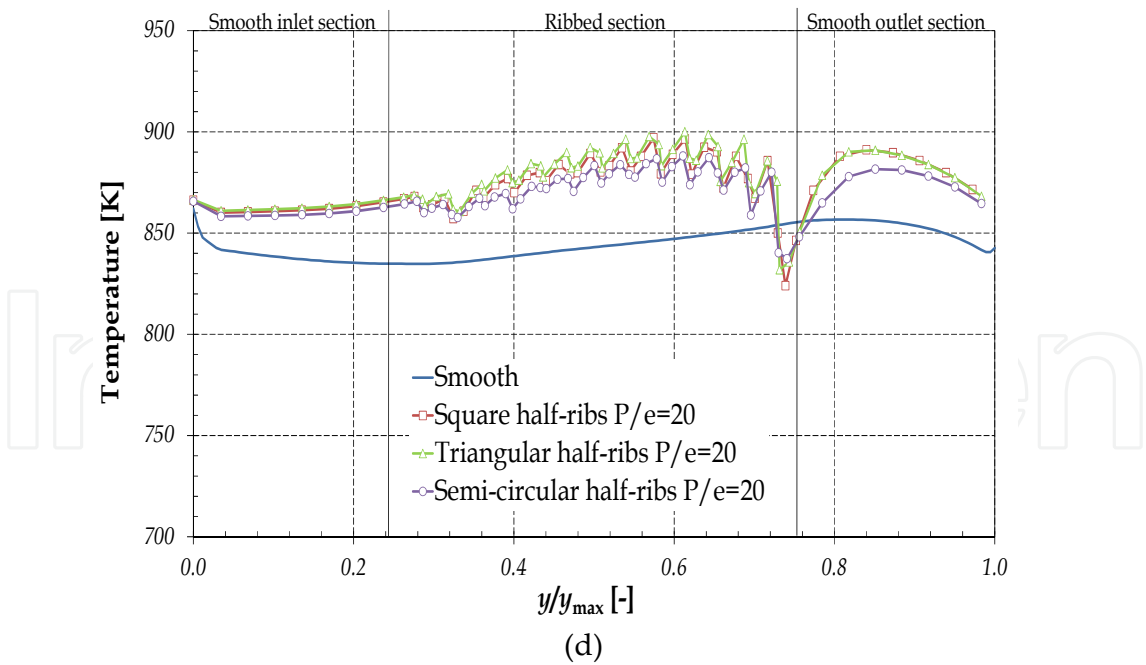
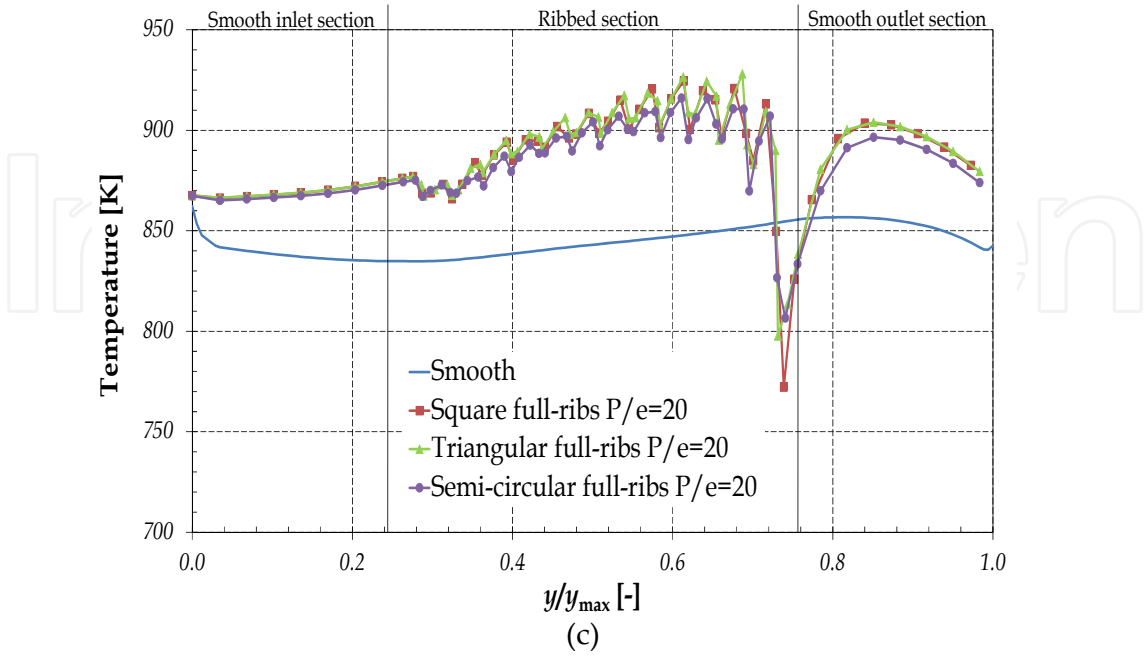


Figure 11. Temperature distribution at the centerline inside of the central cooling channel

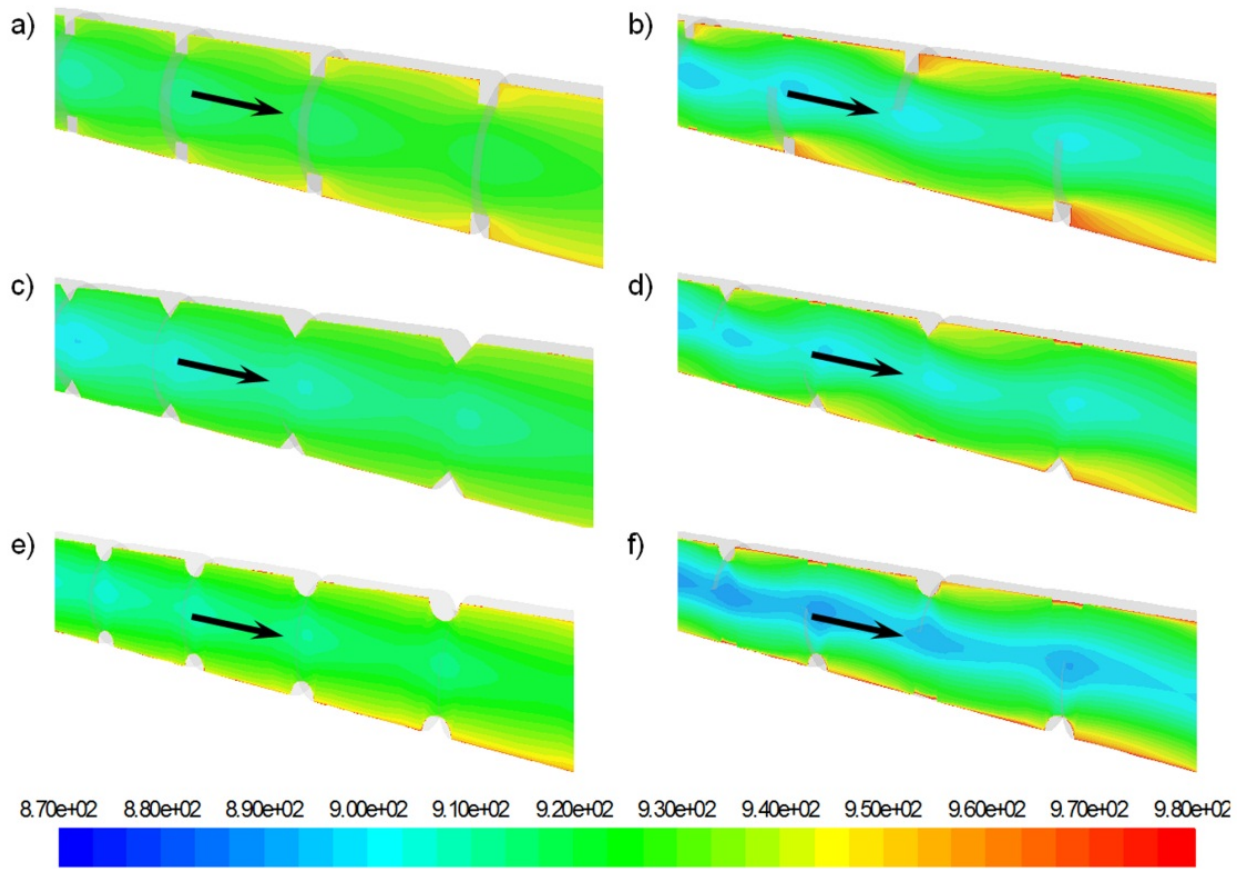


Figure 12. Temperature Contours [K] along the central cooling channel for the different types of ribs with $P/e = 10$

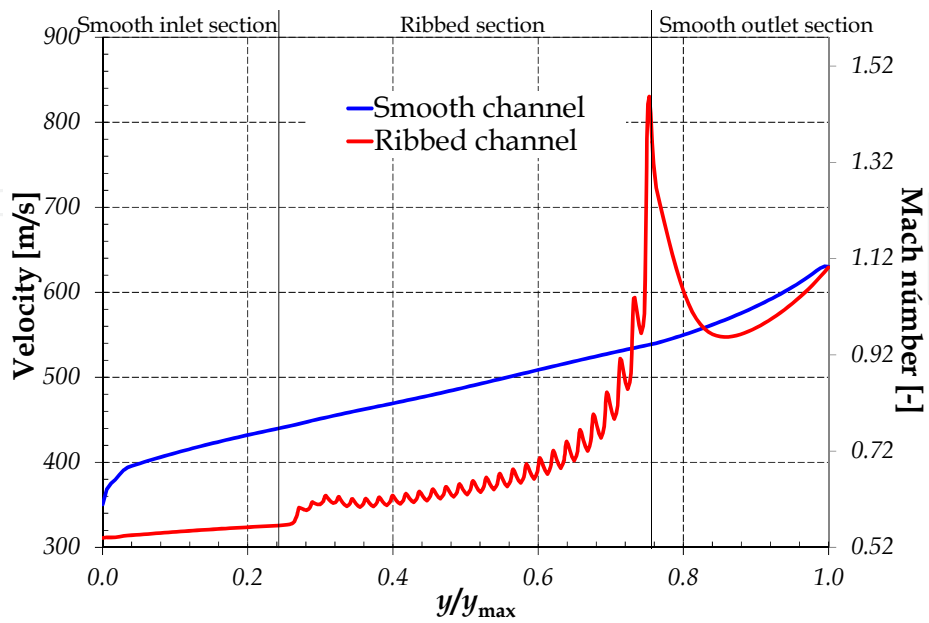


Figure 13. Velocity magnitude [m/s] and Mach number distributions along the centreline inside of the central cooling channels.

In order to have a better description of the effects caused by the acceleration and deceleration of the flow mentioned above, Figure 14 shows the contours of the axial velocity through the central cooling channel at a longitudinal plane. Figures 14a, 14c and 14e show the results for the different types of full-ribs. Figures 14b, 14d and 14f show the results for the half-ribs, both models have a ratio of $P/e = 10$. As it can be observed, the flow is strongly accelerated every time that it passes between the rib tips, which provoke that the fluid increases its velocity due to area reduction. Then, the area increases again to decelerate the fluid flow. These fluctuations of acceleration are presented periodically in the cooling channel, generating variations in the flow parameters. This effect is more noticeable in the cases of half-ribs, having the higher bulk velocity in the channel at each rib. Also, the higher velocity is extended downstream of the ribs tip, where the flow follows a wavy path in the bulk section of the channel. Also, it is observed that in the half-rib cases, the flow is forced towards the surface of the opposite rib.

On the other hand, the square and semi-circular ribs produce recirculation zones as well as stagnation points over the upstream and downstream rib surfaces, respectively. The triangular ribs only produce recirculation zones in the downstream surfaces. These effects are similar to configurations with a ratio of $P/e = 20$.

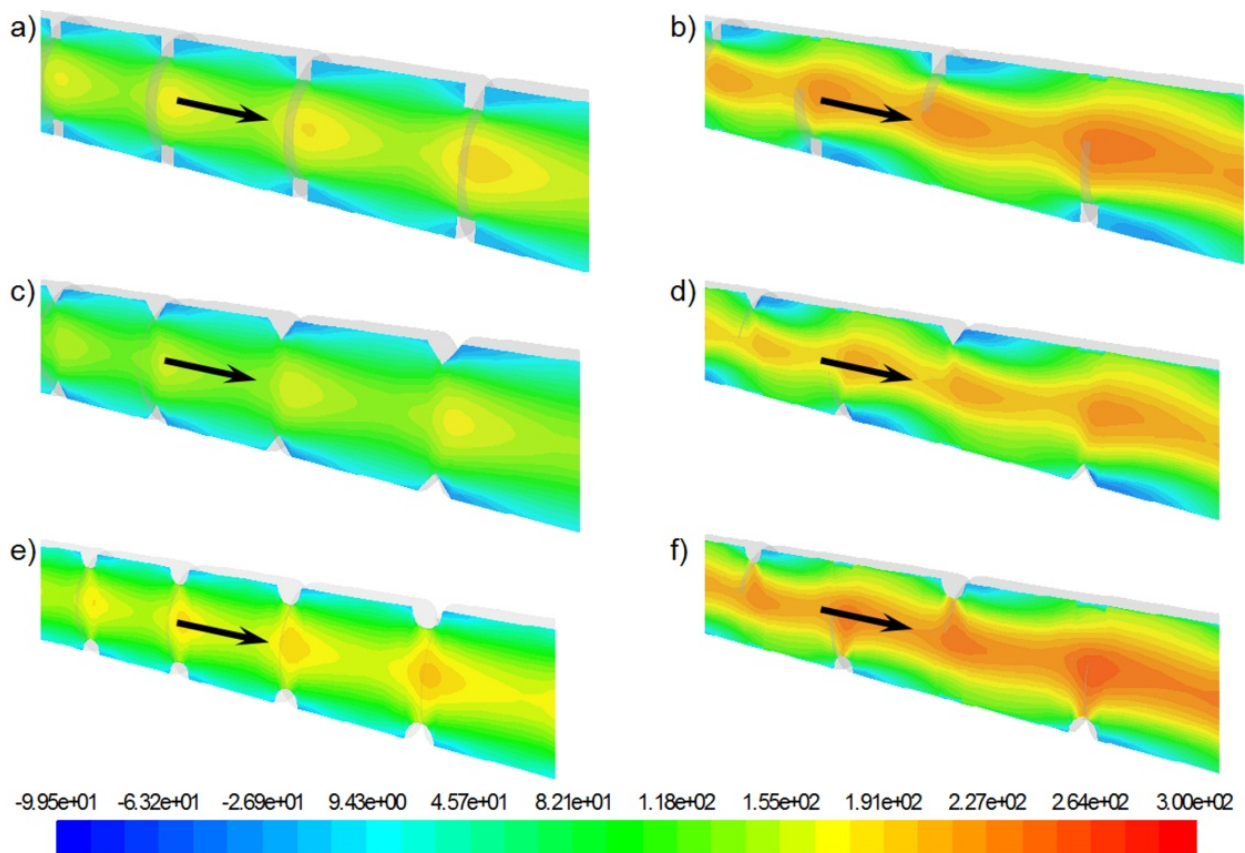


Figure 14. Contours of axial velocity [m/s] along to central cooling channel for the different types of ribs with $P/e = 10$

Pressure loss

The local static pressure is presented in terms of the normalized pressure difference, calculated by the equation (19)

$$\Delta p = \frac{p - p_{exit}}{0.5\rho u^2} \quad (19)$$

where p is the local static pressure, p_{exit} is the pressure at the outlet of the cooling channel, where the cooling air is mixed with the hot combustion gases and the average velocity u is calculated by the channels mass flow rate. Figures 15 and 16 show the local normalized static pressure distribution for the different rib configurations with an aspect ratio, P/e , of 10 and 20, respectively.

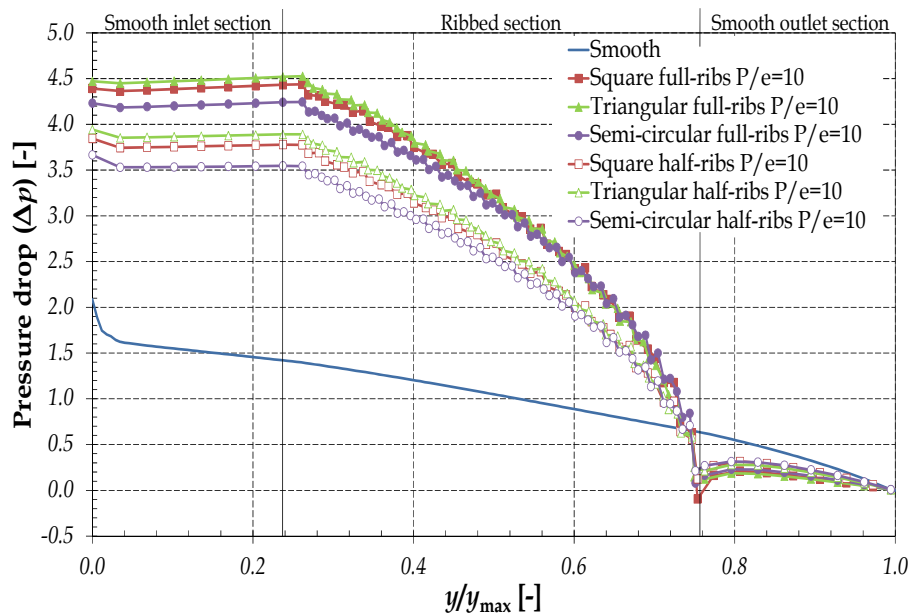


Figure 15. Static pressure distribution along the central cooling channel for different types of ribs with $P/e = 10$

In Figures 15 and 16 can be observed that the slope of pressure drop in the smooth inlet section decreases due to a gradual reduction of channel cross-section. This area reduction is localized in the joint between the plenum and the blade. After this section, the pressure increases while the channel distance increases to the ribbed section. This is produced by the stagnation point when the flow shocks with the first ribs. In the ribbed section, the slope of the pressure drop becomes unstable, presenting periodical increments and decrements due to the cross-section variation, producing accelerations and decelerations of the flow. At the smooth outlet section, the slope of the pressure drop is relatively higher than that in the smooth inlet section. This is due to the increase of the flow velocity at this zone due to the rotational force, ejecting the flow inside the hot gases stream in the tip of the blade.

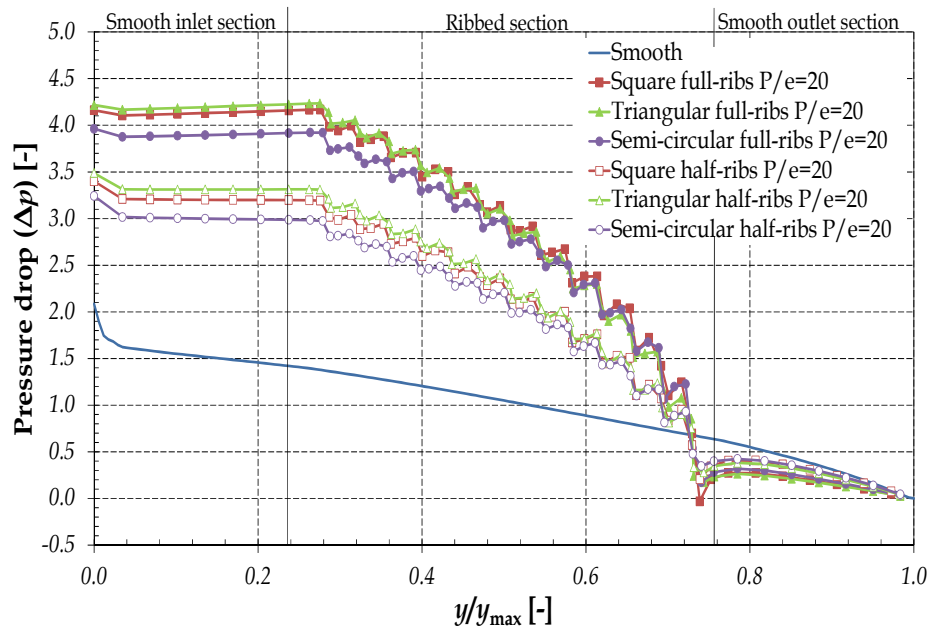


Figure 16. Static pressure distribution along the central cooling channel for different types of ribs with $P/e = 20$

3.3. Temperature distribution inside the blade body

Figure 17 shows the temperature contours at a transversal plane of the blade body right in the middle of the blade for the cases with smooth and full-rib channels with a $P/e = 10$. Comparing the results obtained, it is possible to observe an improvement in the blade internal cooling, allowing a decrement in the internal surface temperature of the cooling channels. Thus, the heat removed by the coolant is increased.

As can be seen in Figure 17, the maximum temperature decreases, approximately about 10 to 20 degrees and is reached close to the internal surfaces for the cases of blade with ribbed channels (Figures 17b, 17c and 17d), noticing that the cooling zone covers the major part of the internal cooling channels, propagating to the leading and trailing edge. In the cases of the blade with smooth channels, it is only present a smaller cooling zone at the three central cooling channels (Figure 17a).

Models with square and triangular cross-section full-ribs show a similar temperature distribution and major heat dissipation compared with the semi-circular full-ribs.

Mazur [16] performed an analysis of a gas turbine bucket failure made of Inconel 738LC super alloy. This bucket operated for 24,000 hours. Mazur et al. [16] found that the maximum stresses are present in the blade cooling channels, producing cracks. Figure 18 shows that kind of cracks. These start in the coating of the cooling channels, propagating and following intergranular trajectories, reaching a depth up to 0.4 mm.

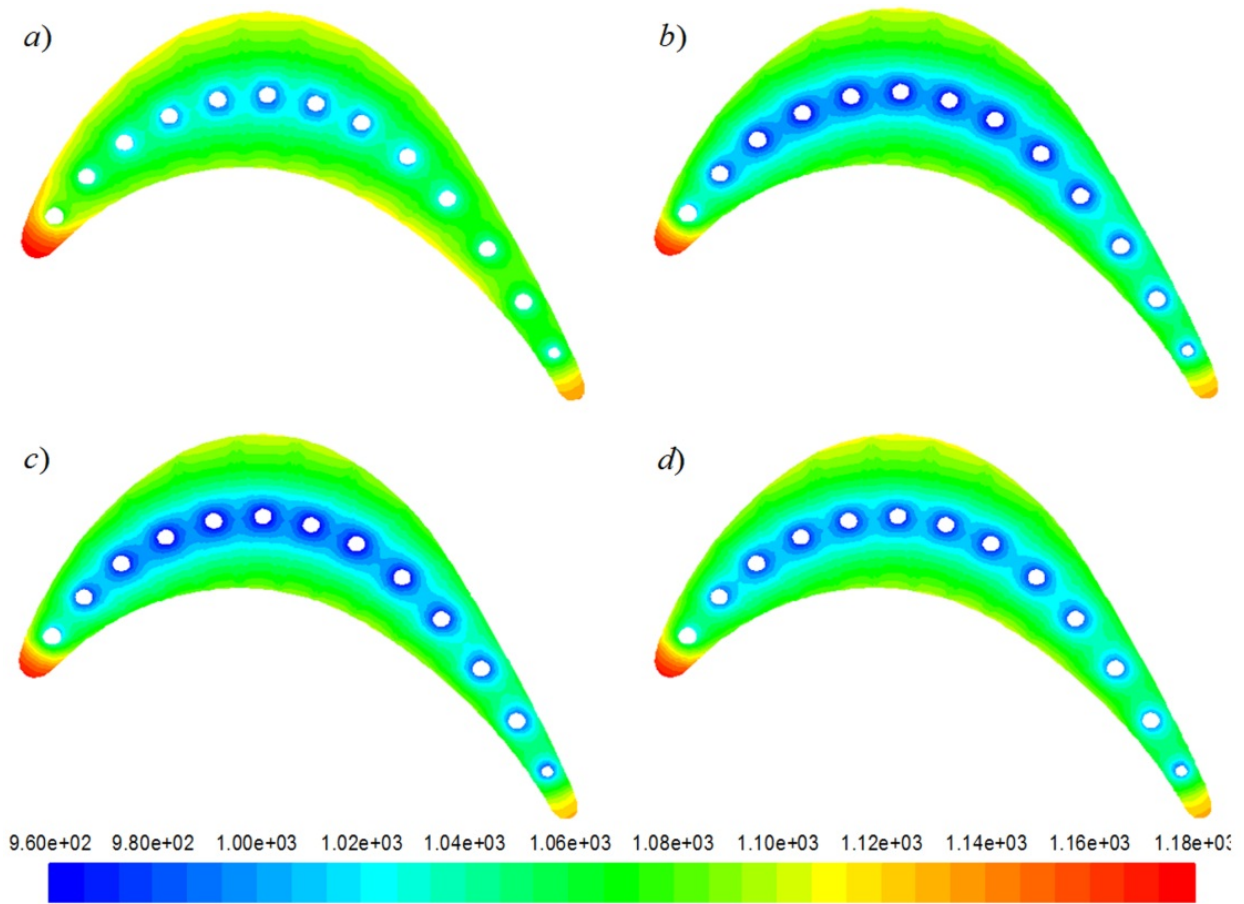


Figure 17. Temperature contours [K] in the metal, a) smooth, b) square full-ribs, c) triangular full-ribs and d) semi-circular full-ribs, cooling channels

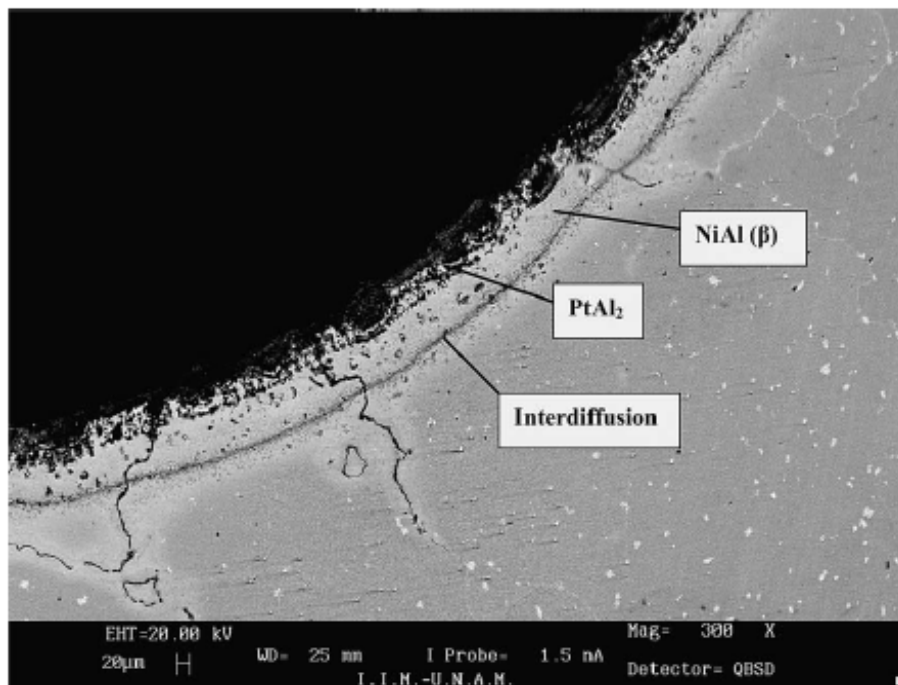


Figure 18. Cracks in the central cooling channels [16]

In this way, the effect generated by increasing the internal cooling zone produces an increment in the useful life of the blade, since the useful life of gas turbine blades is reduced to half with every 10-15 °C rise in metal temperature [2]. On the other hand, the use of ribs increases the heat transfer, generating an increase in thermal gradients at internal surface of cooling channels. In the leading edge another interesting effect is presented. There is a minor penetration of the blade body temperature (Figures 17b to 17d) caused by the use of the ribs. However, it cannot be adequate due to the fact that the thermal gradients at the leading edge are increasing. Due to these thermal effects, these zones must be taken into account to be protected by means of the film cooling method.

Figure 19 shows the blade profile right in the middle along the blade height. In this section, a perpendicular line to the blade chord is created to obtain the temperature distribution inside the solid body as well as in the cooling air through the central cooling channel. The distance is a dimensionless parameter, taking values between 0 and 1, starting in the suction side and ending in the pressure side, respectively.

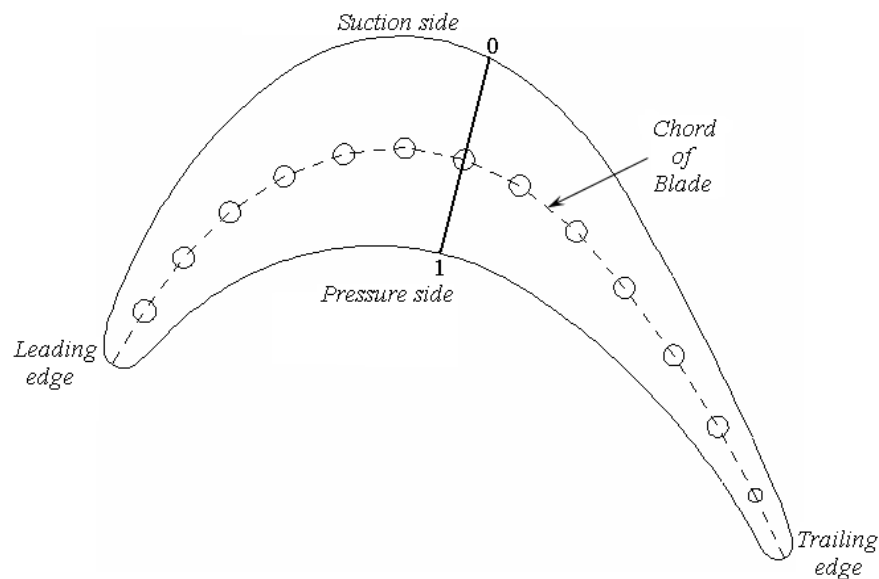


Figure 19. Perpendicular line to the blade chord where data is obtained

In Figures 20a and 20b the temperature distributions for the cases with full and half-ribs are presented, respectively. Both models have an aspect ratio between pitch and height of the ribs (P/e) of 10. Figure 20a shows that the cases of ribbed channels present a significant decrement in the temperatures inside the solid body in comparison with smooth channels. The triangular full-ribs model presents a higher temperature decrement, reaching a temperature decrement up to 20 K closer to the channel surface and 10 K in the pressure and suction sides. Figure 20b shows that square and semi-circular half-ribs do not offer a considerable decrement in the temperature inside the blade body, since the temperature distributions are very similar to the case with smooth cooling channels. The case with triangular half-ribs presents a smaller temperature decrement than the case with triangular full-ribs (Figure 20a). The decrement of temperature achieved by this configuration is between 10 K near to the channel surface and 4 K in the pressure and suction sides. In the

fluid section, the temperature is bigger in all the ribbed cases than in the smooth case, obtaining improved heat dissipation to the cooling air.

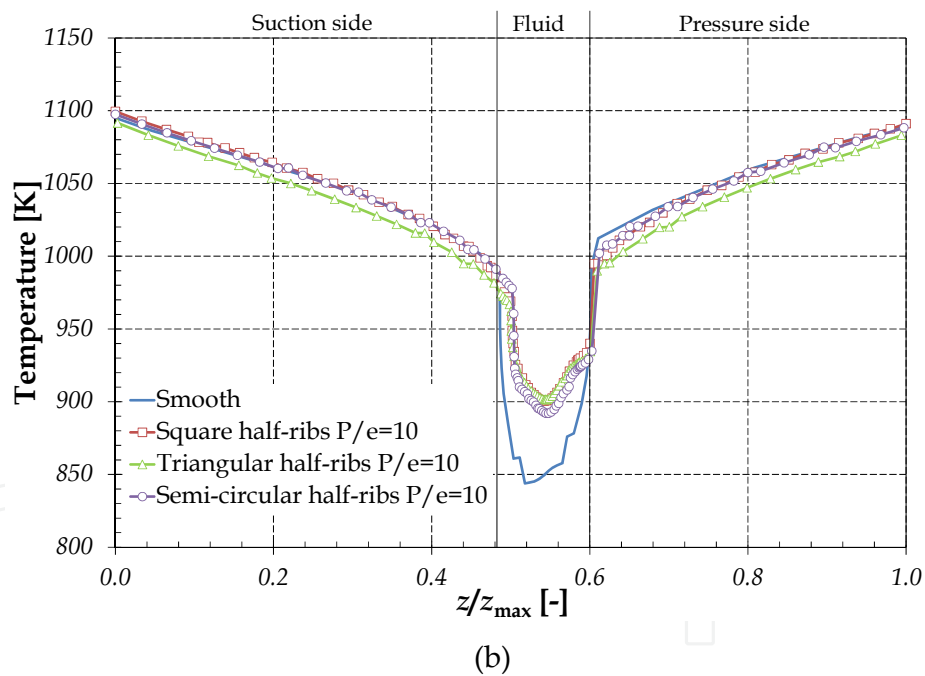
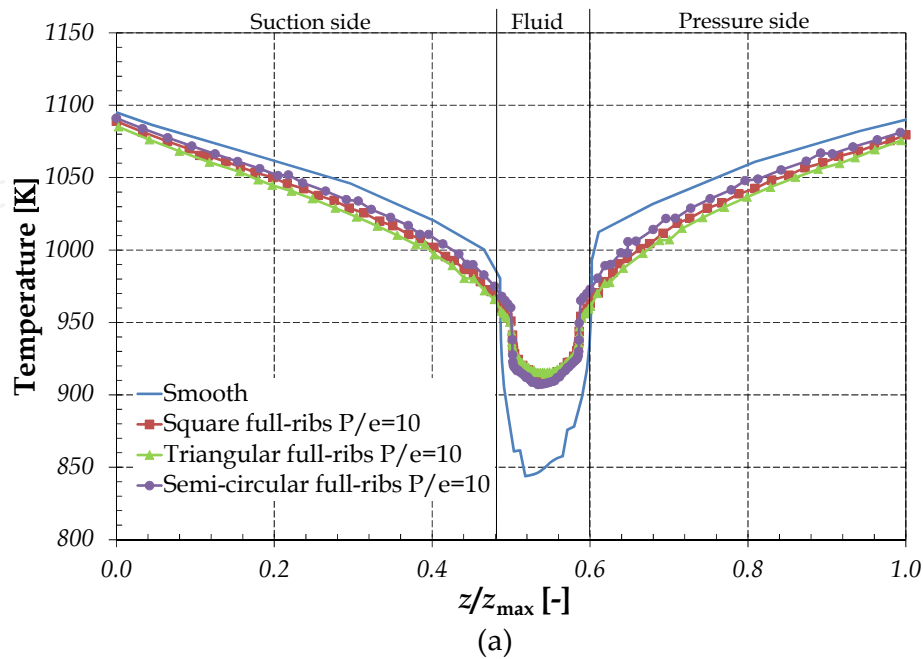


Figure 20. Temperature distributions in the blade with ribbed cooling channels with $P/e = 10$

Figures 21a and 21b show the temperature distributions for the cases of cooling channels with full and half-ribs with an aspect ratio of $P/e = 20$. Figure 21a shows that the temperature distributions in the solid body are similar for the three ribbed cases, having the lowest temperature in the square ribs model. With these configurations a higher penetration of the cooling blade using any rib geometry is achieved. These configurations present a similar behaviour, in comparison with the results presented in Figure 20a. These cases present a

temperature reduction up to 22 K in regions close to the channel surface and up to 10 K in the pressure and suction sides. In Figure 21b can be observed a uniform behaviour of the temperature distribution for the three types of ribs. This behaviour is basically the same for all the cases. However, the blade cooling is affected due to the temperature distributions obtained for all the cases with different tendency to be similar for the smooth case, having a smaller improvement on the blade temperature when compared with the temperature profiles shown in Figure 20b.

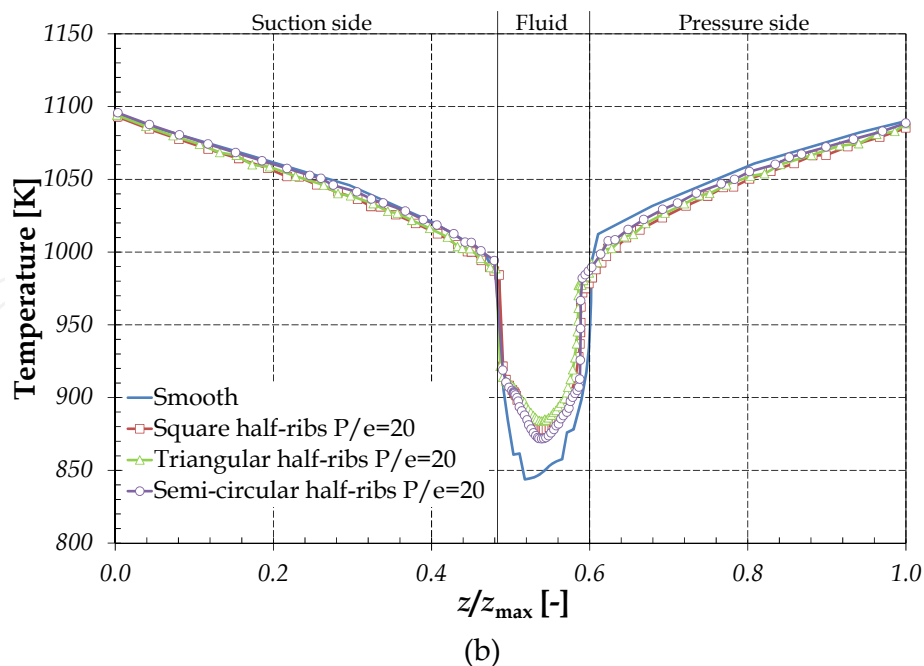
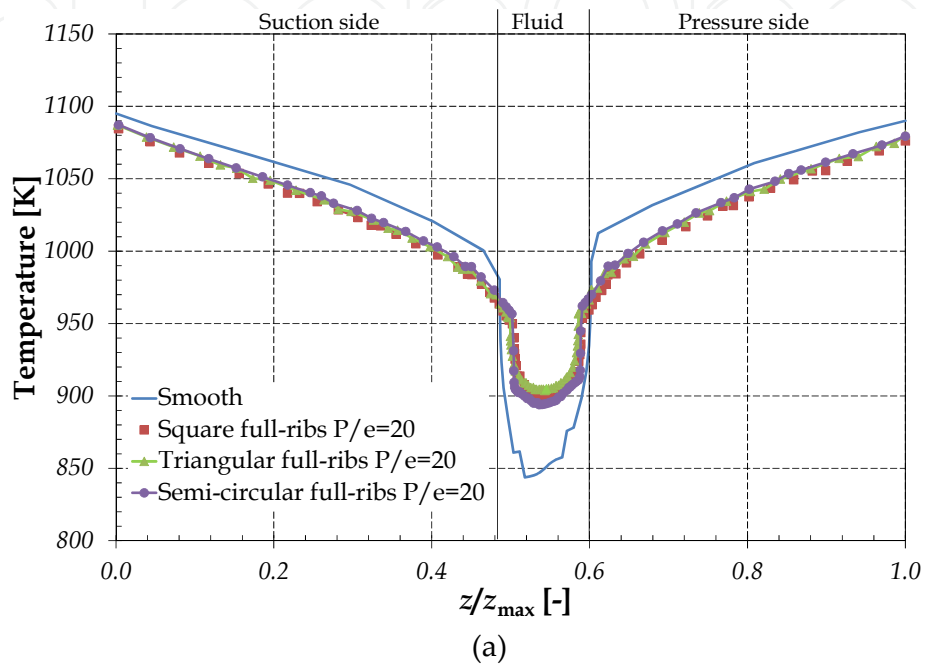


Figure 21. Temperature distributions in the blade with ribbed cooling channels with $P/e = 20$

The temperature distributions of cooling air presented in Figures 20 and 21 have a symmetrical parabolic behaviour due to mixing flow. This is generated by placing ribs, while the profile related with the smooth channel has an asymmetrical behaviour. In this case the profile presents a tendency to attach to the pressure side due to the blade rotational force.

The effect of having a symmetric profile improves the heat transfer from the internal surface of the cooling channels to the air, due to the turbulence generated in the flow which is increased because of the ribs removing a high quantity of heat.

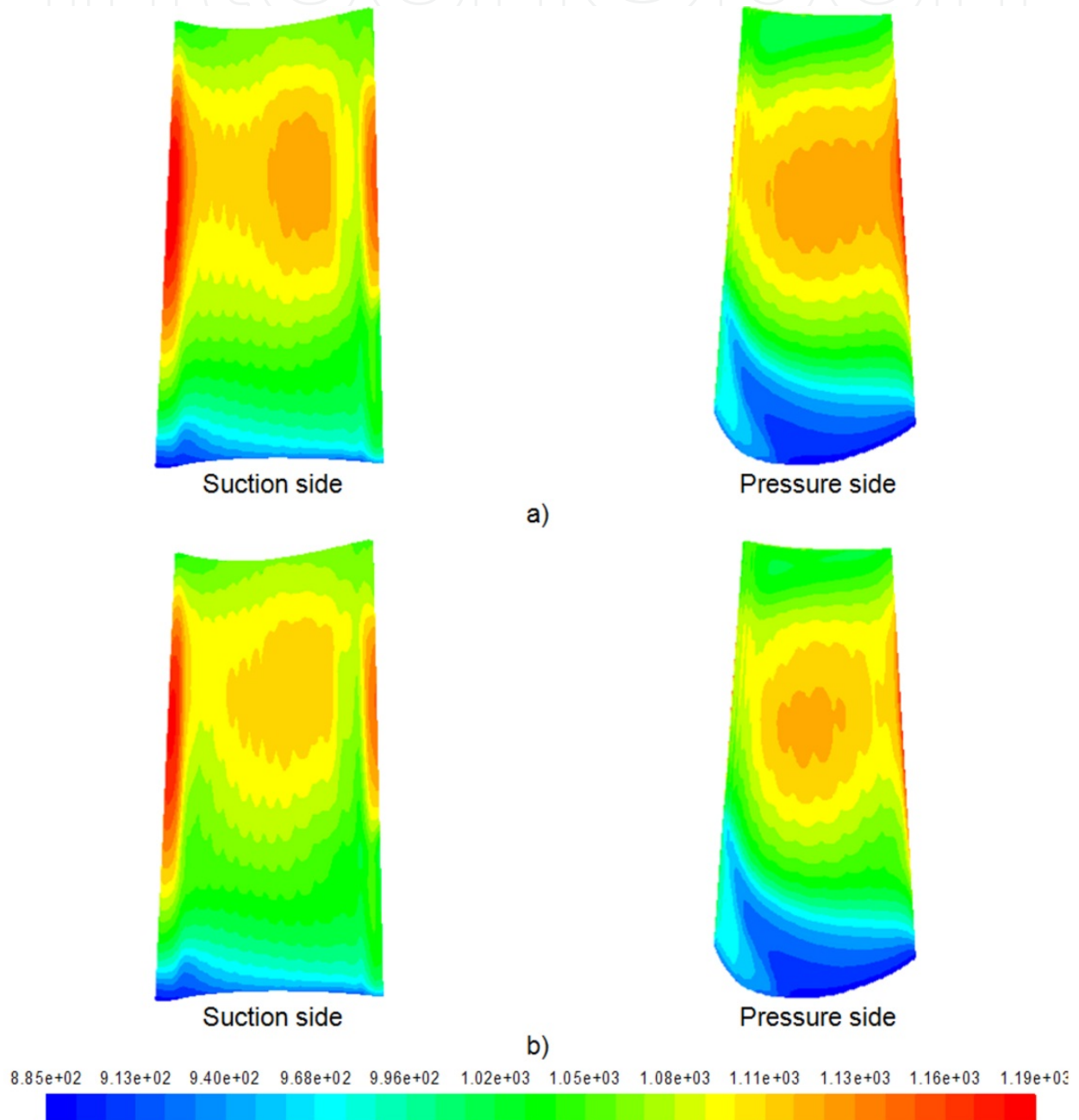


Figure 22. Surface temperature distributions [K] on the blade with a) smooth cooling channel and b) ribbed cooling channels with $P/e = 10$

3.4. Surface temperature distribution in the body blade

Figure 22 shows a comparison between the surface temperature distribution on the pressure side and the suction side of the blade for the cases of models with smooth and ribbed cooling channels. The temperature distributions of the blade with ribbed internal cooling channels correspond to the configuration with square full-ribs with a ratio $P/e = 10$. As can be seen in Figure 22, internal cooling generated by ribs has an effect on the blade surface temperature, since it presented a substantial decrease in surface temperature on the pressure and suction sides of the blade. Also, it is observed a reduction of the spot of maximum temperature on the leading and trailing edges of the blade generated by the parabolic temperature profile at the inlet of the hot combustion gases. Another effect which can be seen is the stain of cooling at the root of the blade on the suction side, which is generated by the flow of air entering the vane platform.

4. Conclusions

In the present work, a numerical study was performed, with the aim to assess the effect generated by the ribs in the temperature distributions inside the blade body as well as the pressure drop through the cooling channels with different types of ribs. The main conclusions are:

The validation of the numerical model by comparing the internal and external flow with experimental [22] and semi-empirical [23, 24] data was developed. The pressure drop in the internal flow obtained through the numerical solution and semi-empirical [23, 24] data, offers a close enough agreement, with an absolute difference of 3.25%.

The higher and smaller temperatures of the internal flow are presented for the configurations of full-ribs in the ribbed section, reaching temperatures from 937 K to 741 K, respectively, while the half-ribs configurations offer a smaller difference of temperature in this section. This range is between temperature of 927 K and 791 K. The configurations of full-ribs have a larger contact area than configurations of half-ribs. Due to this reason, the configurations of full-ribs remove more thermal energy from the blade body.

The configuration with full-ribs with $P/e = 20$, offers the best cooling with any rib type. This could be due to the fact that the flow has a high recirculation zone between the ribs, generating a hydrodynamic perturbation to provoke a separation of the boundary layer.

The acceleration and deceleration effects, which are presented in the ribbed section, play an important role in the flow behaviour of the compressible fluid, since the high velocity of the flow shows a strong influence on the variations of temperature in the flow field. The highest Mach number and velocity are obtained with the ribbed channel, whose values are 1.45 and 823 m/s, respectively, while that smooth channel presents a continuous acceleration of the flow along the channels.

The ratio between the required inlet pressure in the cooling channels and the outlet pressure increases from 4 to 4.5 times approximately for the cases with full-ribs with aspect ratios

(P/e) of 10 and 20, respectively. For the half-ribs, this ratio is between 3 to 4 times, approximately. These values are higher than the values obtained in smooth cooling channels.

The ribbed cooling channels present different pressure drops, ordered from higher to lower pressure drops, they are triangular, square and semi-circular ribs, respectively. The triangular ribs offer the highest cooling effects of the analyzed cases; however, this configuration presents the highest pressure drop when compared with any other case.

The turbulence promoters allow to obtain a maximum temperature decrease, approximately about 10 to 20 degrees, close to the internal surfaces of the blade body. This allows reducing damages by fatigue and thermal stresses.

Author details

Armando Gallegos-Muñoz, Nicolás C. Uzárraga-Rodríguez and Francisco Elizalde-Blancas
Department of Mechanical Engineering, University of Guanajuato, Salamanca, Gto., Mexico

5. References

- [1] Je-Chin Han, Sandip Dutta, Srinath Ekkad (2000) Gas Turbine Heat Transfer and Cooling Technology. Chapter 1, 1-10. Taylor and Francis.
- [2] A. K. Sleiti, J. S. Kapat (2006) Comparison between EVM and RSM Turbulence Models in Predicting Flow and Heat Transfer in Rib-Roughened Channels. *Journal of Turbulence*. 7(29): 1-21.
- [3] Marcel León de Paz, B.A. Jubran (2011) Numerical Modeling of Multi Micro Jet Impingement Cooling of a Three Dimensional Turbine Vane. *Heat Mass Transfer*. 47: 1561-1579.
- [4] Hojjat Saberinejad, Adel Hashiehba, Ehsan Afrasiabian (2010) A Study of Various Numerical Turbulence Modeling Methods in Boundary Layer Excitation of a Square Ribbed Channel. *World Academy of Science, Engineering and Technology*. 71: 338-344.
- [5] N. Cristobal Uzarraga-Rodríguez, Armando Gallegos-Muñoz, J. Cuauhtemoc Rubio-Arana, Alfonso Campos-Amezcuca Mazur Zdzislaw (2009) Study of the Effect of Turbulence Promoters in Circular Cooling Channels. *Proceedings of 2009 ASME Summer Heat Transfer Conference*. 1: 1-14.
- [6] Gongnan Xie, Weihong Zhang, Bengt Sunden (2012) Computational Analysis of the Influences of Guide Ribs/Vanes on Enhanced Heat Transfer of a Turbine Blade Tip-Wall. *International Journal of Thermal Sciences*. 51: 184-194.
- [7] Kyung Min Kim, Hyun Lee, Beom Seok Kim, Sangwoo Shin, Dong Hyung Lee, Hyung Hee Cho (2009) Optimal Design of Angled Rib Turbulators in a Cooling Channel. *Heat Mass Transfer*. 45: 1617-1625.
- [8] Mushatet Khudheyer S. (2011) Simulation of Turbulent Flow and Heat Transfer Over a Backward-Facing Step with Ribs Turbulators. *Thermal Science*. 15: 245-255.

- [9] Smith Eiamsa-ard, Wayo Changcharoen (2011) Analysis of Turbulent Heat Transfer and Fluid Flow in Channels with Various Ribbed Internal Surfaces. *Journal of Thermal Science*. 20: 260-267.
- [10] Hossein Shokouhmand, Mohammad A. Esmaeili Koohyar Vahidkhah (2011) Numerical Simulation of Conjugated Heat Transfer Characteristics of Laminar Air Flows in Parallel-Plate Dimpled Channels. *World Academy of Science, Engineering and Technology*. 73: 218-225.
- [11] Pongjet Promvong, Withada Jedsadaratanachai, Sutapat Kwankaomeng, Chinruk Thianpong (2012) 3D Simulation of Laminar Flow and Heat Transfer in V-Baffled Square Channel. *International Communications in Heat and Mass Transfer*. 39: 85-93.
- [12] H. K. Versteeg, W. Malalasekera (1995) *An Introduction to Computational Fluid Dynamics*. Chapter 2, 10-26. Longman Scientific & Technical.
- [13] Fluent Inc. Products (2006). *FLUENT 6.3 Documentation User's Guide*.
- [14] Gambit 2.4.6 (2006). *Fluent Inc. Products Documentation User's Guide*.
- [15] A. Campos Amezcua, A. Gallegos Muñoz, Mazur Z., Vicente Pérez, Arturo Alfaro-Ayala, J.M. Riesco-Avila, J.J. Pacheco-Ibarra (2007a) Análisis Dinámico-Térmico-Estructural de un Alabe de Turbina de Gas con Enfriamiento Interno. 4to. Congreso Internacional, 2do Congreso Nacional de Métodos Numéricos en Ingeniería y Ciencias Aplicadas UMSNH-SMMNI-CIMNE, 1: 1-11.
- [16] Z. Mazur, R. A. Luna, I.J. Juarez, A. Campos (2005) Failure Analysis of a Gas Turbine made of Inconel 738LC Alloy. *Engineering Failure Analysis*. 12: 474-486.
- [17] Nicolás C. Uzárraga-Rodríguez (2009) Análisis de Promotores de Turbulencia para mejorar el Enfriamiento en Álabes de Turbinas de Gas. Thesis.
- [18] A. Campos-Amezcua (2007b) Análisis y Optimización Termomecánica, en Estado Transitorio, de la Primera Etapa de Alabes en una Turbina de Gas con Enfriamiento Interno. Thesis.
- [19] Frank P. Incropera, David P. DeWitt, Theodore L. Bergman, Theodore L. Bergman (2007) *Fundamentals to Heat and Mass Transfer*, 6th Ed.. Appendix A, Table A.4, page 941. John Wiley.
- [20] S. V. Patankar (1980) *Numerical Heat Transfer and Fluid Flow*. Chapter 2, 11-24. Hemisphere..
- [21] B. E. Launder, D. R. Spalding (1974) The Numerical Computation of Turbulent Flow. *Computer Methods in Applied Mechanics and Engineering*. 3(2): 269-289. Elsevier
- [22] J. S. Kwak, J. Ahh J., Han, Lee, C. Pang, R. S. Bunker, R. Boyle, R. Gaugler (2003) Heat Transfer Coefficient on the Squealer Tip and Near Squealer Tip Region of Gas Turbine Blade. *Journal of Turbomachinery*. 125: 778-787.
- [23] J. Nikuradse (1937) *Law of Flow in Rough Pipes*. National Advisory Commission for Aeronautics, Washington, DC, USA.
- [24] R. L. Webb, E.R.G. Eckert, R.J. Goldstein (1971) Heat Transfer and Friction in Tubes with Repeated-Rib Roughness. *International Journal of Heat and Mass Transfer*. 14: 601-617.
- [25] Yunus A. Cengel, M. A. Boles (2006) *Thermodynamics an Engineering Approach*, 5th Ed.. Chapter 17, Figure 17-52, page 862. McGraw Hill.